

Synchronization of neuromorphic memristive Josephson junction network and its application

Dejun Yan(严德军), Fuqiang Wu(吴富强), and Wenshuai Wang(汪文帅)
Citation: Chin. Phys. B, 2026, 35 (**1**): 010505. DOI: 10.1088/1674-1056/ae1456
http://cpb.iphy.ac.cn; http://iopscience.iop.org/cpb

What follows is a list of articles you may be interested in

Design of a memristive chaotic map and its adaptive regulation

Ya Wang(王亚), Xin-Lin Song(宋欣林), and Fei-Fei Yang(杨飞飞)
Chin. Phys. B, 2025, 34 (**9**): 090504. DOI: 10.1088/1674-1056/adea5c

Dynamical behaviors of a multifunctional neural circuit

Xiao-Hong Gao(高晓红), Kai-Long Zhu(朱凯龙), and Fei-Fei Yang(杨飞飞)
Chin. Phys. B, 2025, 34 (**9**): 090503. DOI: 10.1088/1674-1056/ae001b

Detection of EEG signals in normal and epileptic seizures with multiscale multifractal analysis approach via weighted horizontal visibility graph

Lu Ma(马璐), Yan-Lin Ren(任彦霖), Ai-Jun He(何爱军), De-Qiang Cheng(程德强), and Xiao-Dong Yang(杨小冬)
Chin. Phys. B, 2023, 32 (**11**): 110506. DOI: 10.1088/1674-1056/acdfbf

Energy spreading, equipartition, and chaos in lattices with non-central forces

Arnold Ngapasare, Georgios Theocharis, Olivier Richoux, Vassos Achilleos, and Charalampos Skokos
Chin. Phys. B, 2022, 31 (**2**): 020506. DOI: 10.1088/1674-1056/ac3a5e

Nonlinear dynamics analysis of cluster-shaped conservative flows generated from a generalized thermostatted system

Yue Li(李月), Zengqiang Chen(陈增强), Zenghui Wang(王增会), and Shijian Cang(仓诗建)
Chin. Phys. B, 2022, 31 (**1**): 010501. DOI: 10.1088/1674-1056/ac0a61

SPECIAL TOPIC — Biophysical circuits: Modeling & applications in neuroscience

Synchronization of neuromorphic memristive Josephson junction network and its application

Dejun Yan(严德军)[1], Fuqiang Wu(吴富强)[1,2,†], and Wenshuai Wang(汪文帅)[1]

[1] *School of Mathematics and Statistics, Ningxia University, Yinchuan* 750021, *China*
[2] *Ningxia Basic Science Research Center of Mathematics, Yinchuan* 750021, *China*

(Received 12 September 2025; revised manuscript received 14 October 2025; accepted manuscript online 17 October 2025)

Neuromorphic circuits based on superconducting tunnel junctions have attracted much attention due to their high-speed computing capabilities and low energy consumption. Josephson junction circuits can effectively mimic biological neural dynamics. Leveraging these advantages, we construct a Josephson junction neuron-like model with a phase-dependent dissipative current, referred to as a memristive current. The proposed memristive Josephson junction model exhibits complex dynamical behaviors. Furthermore, considering the effect of a fast-modulated synapse, we explore synchronization phenomena in coupled networks under varying coupling conductances and excitatory/inhibitory interactions. Finally, we extend the neuromorphic Josephson junction model — exhibiting complex dynamics — to the field of image encryption. These results not only enrich the understanding of the dynamical characteristics of memristive Josephson junctions but also provide a theoretical basis and technical support for the development of new neural networks and their applications in information security technology.

Keywords: nonlinear dynamics, memristive Josephson junction, synchronization, image encryption

PACS: 05.45.Pq, 05.45.Gg, 05.45.Xt

DOI: 10.1088/1674-1056/ae1456 **CSTR:** 32038.14.CPB.ae1456

1. Introduction

A neuromorphic electronic circuit is a rapidly advancing device that employs neuro-dynamics-inspired concepts to implement circuits of biophysical neurons and synapses. Numerous neuromorphic circuits involve memristors and Josephson junctions.[1–5] Biophysical neuronal systems generate oscillatory behaviors including spiking, bursting, and chaotic firing.[6–9] The neuronal network, coupled with synapses, can oscillate synchronously. The memristive coupled neuron model, based on the effect of electromagnetic induction, can modulate excitability and induce different types of firing patterns.[10–13] The memristive neuron-inspired circuit with negative differential resistance can be used to emulate a wide range of firing patterns.[14–18]

Neuromorphic circuits involving Josephson junctions present several advantages, including storage, processing speed, memory, and reduced energy consumption. Josephson junctions, discovered in the early 1960s, remain at the forefront of advancing technology in superconducting electronics.[19–21] Josephson junctions are employed in quantum computing and neuromorphic systems. The resistively and capacitively shunted junction model has the natural capability of mimicking excitability and spiking behavior.[22] An electronic circuit model with two Josephson junctions can reproduce many neuron-like characteristic behaviors, including action potentials, refractory periods, firing thresholds, excitability, and chaos.[23,24] The memristive Josephson junction based on different superconducting materials has been proposed[25] and is employed to generate neuron-like excitability and spiking.[26] The memristive Josephson junction coupled with an inductor can mimic bursting patterns with the same bifurcation mechanism as the Hindmarsh–Rose model. Many circuits involving Josephson junctions have been developed in neuromorphic systems.[27–30] Coupled Josephson junctions with a resistive effect can exhibit near-complete synchronization for sufficiently strong coupling.[31] Josephson junction arrays with different coupling schemes display a wide range of collective behaviors, including spatiotemporal patterns, spiral waves, and target waves.[32–36] Josephson junction circuits can display complex oscillatory behaviors, including chaotic modes.[37–39] Chaotic series with complex dynamics have garnered significant attention due to their extreme sensitivity to initial parameters and excellent pseudo-random characteristics.[40–42] However, many encryption schemes relying on simple chaotic systems suffer from security vulnerabilities, including limited key space, susceptibility to plaintext/ciphertext attacks, and dynamic degradation under finite-precision computations. To address these challenges, researchers are increasingly turning to chaotic systems with more complex dynamics. Chaotic Josephson junctions have been proposed for implementing image encryption.[43–45]

†Corresponding author. E-mail: alexwutian@nxu.edu.cn

© 2026 Chinese Physical Society and IOP Publishing Ltd. All rights, including for text and data mining, AI training, and similar technologies, are reserved.

Neuromorphic Josephson junctions attract attention for mimicking neurophysiological properties. There are similarities in the nonlinear dynamics between Josephson junctions and neuronal circuits. Given the memristive effect in superconductors,[25] we propose an improved Josephson junctions neuron model inspired by Ref. [24] and conduct a comprehensive analysis of its nonlinear dynamics, revealing diverse firing patterns and pathways to chaos. Furthermore, we construct a neural network with fast-modulated synaptic interconnections and investigate its synchronization dynamics. Finally, we develop a DNA image encryption scheme with enhanced performance and security by leveraging the excellent chaotic sequences generated by the models.

The remainder of this paper is organized as follows. Section 2 presents the mathematical models of the memristive Josephson junction neuronal network based on a single memristive Josephson junction neuron-like circuit. Section 3 analyzes the dynamical behavior of the single memristive Josephson junction neuronal circuit system, and numerically investigates the synchronization dynamics of the memristive Josephson junction neuronal network. Section 4 analyzes the application of the network system in image encryption. Section 5 concludes the paper.

2. Model description and method

2.1. Modeling of the single memristive Josephson junction neuron

Josephson junctions, composed of two superconductors separated by a thin insulating barrier, are nonlinear superconducting elements. According to the reported work,[24] the circuit involving two Josephson junctions and two inductors attempts to mimic key neuronal behaviors, as shown in Figs. 1(a) and 1(b). For an ideal Josephson junction, the resistively and capacitively shunted junction model, shown in Fig. 1(c), is given by Kirchhoff's law as

$$\begin{cases} C\dfrac{\mathrm{d}V}{\mathrm{d}t} = I - \dfrac{V}{R} - I_{\mathrm{c}}\sin\theta, \\ \dfrac{\hbar}{2e}\dfrac{\mathrm{d}\theta}{\mathrm{d}t} = V, \end{cases} \tag{1}$$

where V is the voltage drop across the junction. θ represents the phase difference between the order parameters of the two superconducting electrodes. A tunnel barrier between two superconductors produces a non-dissipative current called the Josephson current $I_{\mathrm{S}} = I_{\mathrm{c}}\sin\theta$, where I_{c} is the critical current. The quasiparticle dissipative current is described as $I_{\mathrm{R}} = V/R$. t represents time, and e and $\hbar$ denote the electron charge and Planck's constant, respectively.

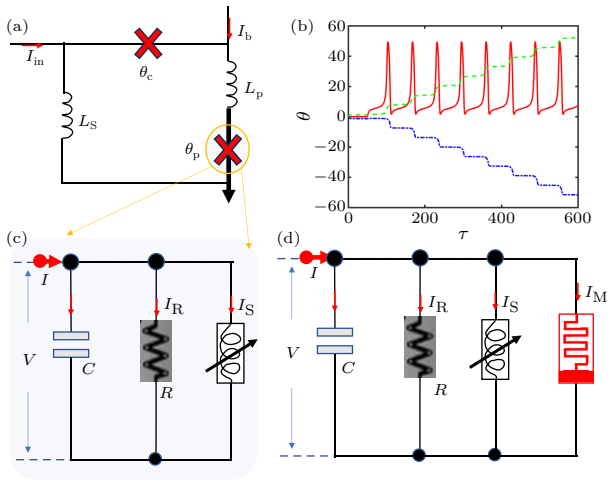


Fig. 1. Neuromorphic circuit schematic. (a) Josephson junction neuron circuit with two inductors. (b) Emulated neuromorphic spiking represented by the total phase difference (red solid line), compared with the pulse junction phase (green dashed line) and the control junction phase (blue dashed line). (c) Equivalent circuit of a Josephson junction, including the resistor R, capacitor C, Josephson current I_{S}, and quasiparticle dissipative current I_{R}. (d) Enhanced equivalent circuit with an additional phase-dependent dissipative current, referred to as the memristive current I_{M}.

Inspiring the previously proposed Josephson junction neuronal model in Ref. [26], we introduce a phase-dependent dissipative current, redefined as the memristive current in Ref. [25], into the shunted junction model in Ref. [22]. The memristive shunted junction model, as depicted in Fig. 1(d), is rewritten as

$$\begin{cases} C\dfrac{\mathrm{d}V}{\mathrm{d}t} = I - G(1+k_{\mathrm{p}}\cos\theta)V - I_{\mathrm{c}}\sin\theta, \\ \dfrac{\hbar}{2e}\dfrac{\mathrm{d}\theta}{\mathrm{d}t} = V, \end{cases} \tag{2}$$

where k_{p} is the ratio between the phase-dependent conductance and the leakage conductance. Through mathematical manipulation, the memristive Josephson junction model is rewritten as

$$\frac{\hbar C}{2e}\frac{\mathrm{d}^2\theta}{\mathrm{d}t^2} + G(1+k_{\mathrm{p}}\cos\theta)\frac{\hbar}{2e}\frac{\mathrm{d}\theta}{\mathrm{d}t} + I_{\mathrm{c}}\sin\theta = I. \tag{3}$$

Then, by using the following normalizations:

$$\tau^2 = \frac{2eI_{\mathrm{c}}}{\hbar C}t^2,\ \ \Gamma^2 = \frac{\hbar}{2eI_{\mathrm{c}}C}G^2,\ \ i = \frac{I}{I_{\mathrm{c}}}, \tag{4}$$

the dimensionless equation for the phase of the memristive Josephson junction circuit is obtained as

$$\frac{\mathrm{d}^2\theta}{\mathrm{d}\tau^2} + \Gamma(1+k_{\mathrm{p}}\cos\theta)\frac{\mathrm{d}\theta}{\mathrm{d}\tau} + \sin\theta = i. \tag{5}$$

Based on the reported Josephson junction neuronal model in Ref. [24], we propose an improved model incorporating the memristive current. The memristive Josephson junction neuronal model is described by the following second-order non-

linear dimensionless differential equations:

$$\begin{cases} \ddot{\theta}_{\rm p}+\Gamma(1+k_{\rm p}\cos\theta_{\rm p})\dot{\theta}_{\rm p}+\sin\theta_{\rm p}=-\lambda(\theta_{\rm p}+\theta_{\rm c}) \\ \qquad\qquad +\Lambda_{\rm s}i_{\rm in}+(1-\Lambda_{\rm p})i_{\rm b}, \\ \ddot{\theta}_{\rm c}+\Gamma(1+k_{\rm p}\cos\theta_{\rm c})\dot{\theta}_{\rm c}+\sin\theta_{\rm c}=-\lambda(\theta_{\rm p}+\theta_{\rm c}) \\ \qquad\qquad +\Lambda_{\rm s}i_{\rm in}-\Lambda_{\rm p}i_{\rm b}, \end{cases} \tag{6}$$

where the dot notation denotes differentiation with respect to τ. The first derivative of $\theta_{\rm p}$ corresponds to the voltage $U_{\rm p}$ across the pulse junction, and the first derivative of $\theta_{\rm c}$ corresponds to the voltage $U_{\rm c}$ across the control junction. $\theta_{\rm p}$ and $\theta_{\rm c}$ represent the pulse and control junction phases, respectively. λ is the coupling parameter, $i_{\rm in}$ is the input current, $i_{\rm b}$ is the bias current, and Γ is the normalized drag constant. p and s denote the inductance gains of $L_{\rm p}$ and $L_{\rm s}$, respectively. The two core components of this circuit are the pulse junction (p) and the control junction (c). In the simulation, the system parameters are $i_{\rm b}=1.909$, $i_{\rm in}=0.203$, $\Gamma=0.8$, and $\Lambda_{\rm p}=\Lambda_{\rm s}=0.5$, based on Refs. [24–26].

2.2. Modeling of the memristive Josephson junction neuronal network

In the brain, synchronized neuronal electrical activity plays a significant role in neuronal signal transmission and coding. Complex networks can capture these biophysical mechanisms. Dynamical networks comprise interacting units, such as memristive Josephson junction neurons, connected through synaptic coupling schemes. In this section, we introduce the fast threshold modulation scheme as a synaptic component into the network.[46] The dynamic equations of the coupled network system are given as follows:

$$\begin{cases} \ddot{\theta}_{{\rm p}i}+\Gamma(1+k_{\rm p}\cos\theta_{{\rm p}i})\dot{\theta}_{{\rm p}i}+\sin\theta_{{\rm p}i}=-\lambda(\theta_{{\rm p}i}+\theta_{{\rm c}i}) \\ \qquad\qquad +\Lambda_{\rm s}i_{\rm in}+(1-\Lambda_{\rm p})i_{\rm b}+I_{\rm net}, \\ \ddot{\theta}_{{\rm c}i}+\Gamma(1+k_{\rm p}\cos\theta_{{\rm c}i})\dot{\theta}_{{\rm c}i}+\sin\theta_{{\rm c}i}=-\lambda(\theta_{{\rm p}i}+\theta_{{\rm c}i}) \\ \qquad\qquad +\Lambda_{\rm s}i_{\rm in}-\Lambda_{\rm p}i_{\rm b}, \\ I_{\rm net}=-g_{\rm c}(\dot{\theta}_{{\rm p}i}-v_{\rm s})\sum\limits_{j=1}^{N}k_{ij}F(\dot{\theta}_{{\rm p}j}-v_{th}), \end{cases} \tag{7}$$

where the state of the ith neuron is described by the variables $\theta_{{\rm p}i}$ and $\theta_{{\rm c}i}$, and $i=1,2,\ldots,N$ denotes the neuron index. The connectivity matrix k_{ij} characterizes the network architecture and is configured as a chain in this study. The index j iterates over the neurons that are directly connected to the ith neuron. Since the right-hand side of Eq. (7) denotes a current term, $I_{\rm net}$ is introduced to represent the synaptic current with fast threshold modulation. $g_{\rm c}$ represents the coupling conductance, a positive $v_{\rm s}$ indicates an excitatory bias voltage, and a negative $v_{\rm s}$ indicates an inhibitory bias voltage. The nonlinear coupling function is $F(\dot{\theta}_{{\rm p}j}-v_{\rm th})=\tanh(v_{\rm th}-\dot{\theta}_{{\rm p}j})$, where $v_{\rm th}$ denotes the threshold potential that determines neuronal sensitivity. When the membrane potential exceeds the threshold value, a neuron can influence other neurons via the synaptic current. To stabilize the membrane potential, the threshold level is fixed at $v_{\rm th}=0$.

3. Numerical simulation

3.1. Dynamics of the single memristive Josephson junction neuron

To investigate the effects of the parameter $k_{\rm p}$ on the firing patterns of the single memristive Josephson junction neuron, we use MATLAB to perform numerical bifurcation analysis and compute the Lyapunov spectrum of the model.

Figure 2 presents the ISI bifurcation diagram and the Lyapunov exponent spectrum for the parameter $k_{\rm p}$. Specifically, when $k_{\rm p}$ ranges between -0.3 and 0.1, the discharge mode of the memristive Josephson junction neuron changes significantly, exhibiting distinct patterns. As shown in Fig. 2(a), with increasing $k_{\rm p}$, the discharge mode of the neuron model initially exhibits period-2 oscillation. Subsequently, it transitions into a chaotic state after a period-4 bifurcation, and finally returns to period-1 oscillation at $k_{\rm p}=0.057$. Correspondingly, Fig. 2(b) shows four Lyapunov exponent curves associated with the four state variables of the model, where the red curve represents the largest Lyapunov exponent. Combining Figs. 2(a) and 2(b), we observe that the largest Lyapunov exponent is positive in the chaotic regime and negative in the periodic regime. Based on the above analysis, we find that the dynamic characteristics of the memristive Josephson junction neuron model are significantly influenced by the parameter $k_{\rm p}$.

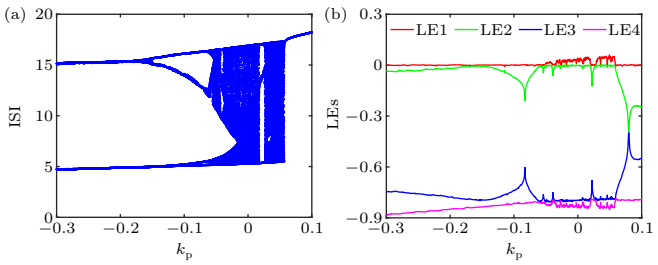


Fig. 2. Dynamical transitions of the memristive Josephson junction neuron. (a) Inter-spike interval (ISI) bifurcation diagram as a function of the parameter $k_{\rm p}$. (b) Lyapunov exponent spectrum corresponding to the parameter $k_{\rm p}$.

In order to further verify the numerical results shown in Fig. 2, we select different values of the parameter $k_{\rm p}$ from Fig. 2(a) and numerically simulate the time series of the state variable $U_{\rm p}$ as well as the phase trajectories of $\dot{\theta}_{\rm p}+\dot{\theta}_{\rm c}$ and the sum of the second derivatives of $\theta_{\rm p}$ and $\theta_{\rm c}$. Figure 3 presents the time series (upper panels) and phase trajectories (lower panels). When the parameter $k_{\rm p}$ is set to -0.2, -0.005, 0.02, and 0.06, respectively, distinct dynamical behaviors emerge. For $k_{\rm p}=-0.2$, the memristive Josephson junction neuron model exhibits spiking-like firing with two peaks. As $k_{\rm p}$ increases to -0.005, the model enters a chaotic state, as illustrated in Figs. 3(b) and 3(f). Furthermore, when

k_p becomes positive, the model displays spiking-like firing with three peaks (Figs. 3(c) and 3(g)) and one peak (Figs. 3(d) and 3(h)) at $k_p = 0.02$ and $k_p = 0.06$, respectively. These observations demonstrate that both positive and negative modulation of the parameter k_p significantly affect the firing patterns of the model. Moreover, the characteristics of the firing patterns agree with the results in Fig. 2, further confirming the correctness of the numerical analysis in Fig. 2.

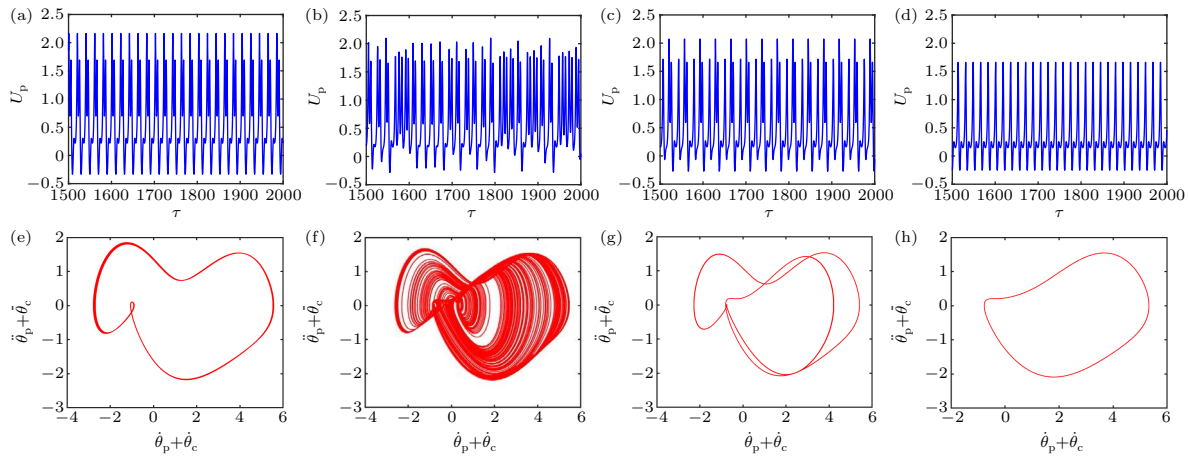


Fig. 3. Time series of the membrane potential and the corresponding phase portraits. (a)–(d) Time series, and (e)–(h) the corresponding phase trajectories. The parameter k_p is set to -0.2, -0.005, 0.02, and 0.06, respectively.

3.2. Synchronization dynamics of the memristive Josephson junction neuronal network

A neuron is the basic unit of a neural network. In this paper, we construct a network composed of 100 memristive Josephson junction neurons and systematically study the dynamic characteristics of the coupling gain parameters. The following formula is used to calculate the degree of synchronization of coupled neural networks:

$$E_{rr} = \left\langle \left(\frac{1}{N} \sum_i \left| \dot{\theta}_{pi} - \overline{\theta}_{prr} \right|^2 \right)^{\frac{1}{2}} \right\rangle_{\Delta T}, \tag{8}$$

where N is the number of neurons, and $\langle \cdots \rangle_{\Delta T}$ denotes a temporal average over a suitable time span. The variable $\bar{\theta}_{prr}$ represents the cluster-averaged value of the vector $\dot{\theta}_{pi}$. After normalization, the values obtained from the above formula lie within $[0, 1]$. The closer the E_{rr} value is to 0, the higher the synchronization degree of the neurons, with 0 indicating complete synchronization; the closer it is to 1, the more asynchronous the neurons are.

Figure 4 shows the synchronization error characteristics of the memristive Josephson junction neural network under different parameter conditions. In the case of the fixed parameter $k_p = 0.06$, we analyze the influence of the coupling conductance parameter g_c and the bias voltage v_s on the synchronization behavior of the network. Specifically, Fig. 4(a) illustrates the effect of the coupling conductance parameter g_c on the synchronization error E_{rr}. As g_c increases, the synchronization error of the network initially increases and then decreases, indicating that increasing the coupling strength within a specific range facilitates the network's transition from an asynchronous state to a synchronous state. This phenomenon highlights the crucial role of coupling strength in enhancing network synchronization. Figure 4(b) shows the effect of the inhibitory bias voltage v_s on the synchronization error. As v_s increases, the network undergoes a transition from synchronization to asynchrony and then back to synchronization. In contrast, as shown in Fig. 4(c), when the network is affected by the excitatory bias voltage, the synchronization error gradually increases with increasing v_s, indicating a transition from a synchronous state to an asynchronous one. These results show that the excitatory bias voltage v_s suppresses network synchronization.

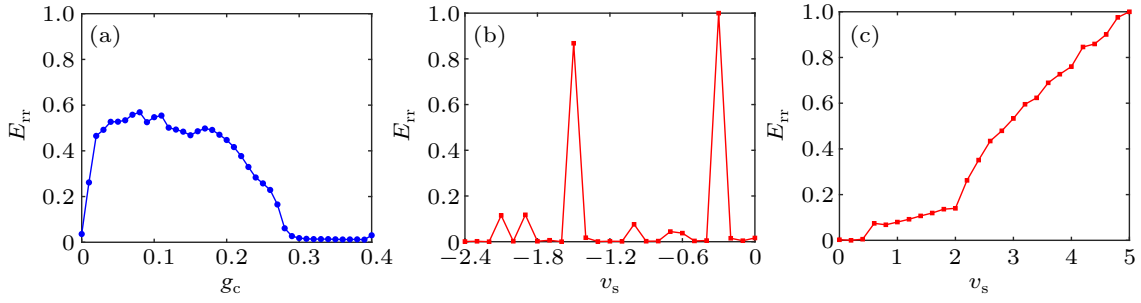


Fig. 4. Synchronization index diagrams. (a) As a function of the coupling conductance g_c. (b) As a function of the inhibitory bias voltage v_s in the range -2.4 to 0. (c) As a function of the excitatory bias voltage v_s in the range 0 to 5. The parameter k_p is set to 0.06.

In summary, Fig. 4 reveals the significant effects of coupling conductance g_c and bias voltage v_s on the synchronization performance of memristive Josephson junction neuronal networks, providing an essential theoretical basis for understanding and regulating the synchronization behavior of neuronal networks.

Figure 5 shows the spatiotemporal patterns and time series of the memristive Josephson junction neural network under different values of the parameter g_c. The values of g_c shown in the figure are 0, 0.1, 0.2, and 0.4, respectively, while the other parameters are fixed as $\Gamma = 0.8$, $\lambda = 0.1$, $\Lambda_p = 0.5$, $i_{in} = 0.203$, $i_b = 1.909$, $v_s = 0$, $k_p = 0.06$, and $\Lambda_s = 0.5$. The time series of the membrane potentials U_p of two representative neurons from different locations in the coupled network are shown in blue ($N = 1$) and red ($N = 100$), respectively. The similarity of the traces reflects the degree of synchronization between the two neurons. In the spatiotemporal pattern diagram, colors indicate instantaneous membrane potential values, with warmer colors corresponding to higher potentials (the excited state) and cooler colors to lower potentials (the resting state). Numerical values in the legend correspond to the actual U_p values obtained in the simulation. It can be seen from Figs. 5(a) and 5(e) that when $g_c = 0$, the neural network exhibits a periodic spike-discharge mode, indicating period-one synchronization behavior. With increasing g_c, as shown in Figs. 5(b) and 5(f), when $g_c = 0.1$, the synchronization of the network is disrupted, and the firing mode becomes irregular, showing a chaotic oscillatory state. Further increasing g_c to 0.2, as shown in Figs. 5(c) and 5(g), the network system initially enters a disordered and unsynchronized state. However, as time progresses, around 700 seconds the network transitions into a synchronized state. This indicates that an appropriate coupling strength can facilitate network synchronization. When g_c is increased to 0.4, as shown in Figs. 5(d) and 5(h), the firing patterns of all 100 neurons become highly consistent, and the network achieves full synchronization. This phenomenon is consistent with the data in Fig. 4(a), further confirming that increasing the coupling parameter promotes network synchronization.

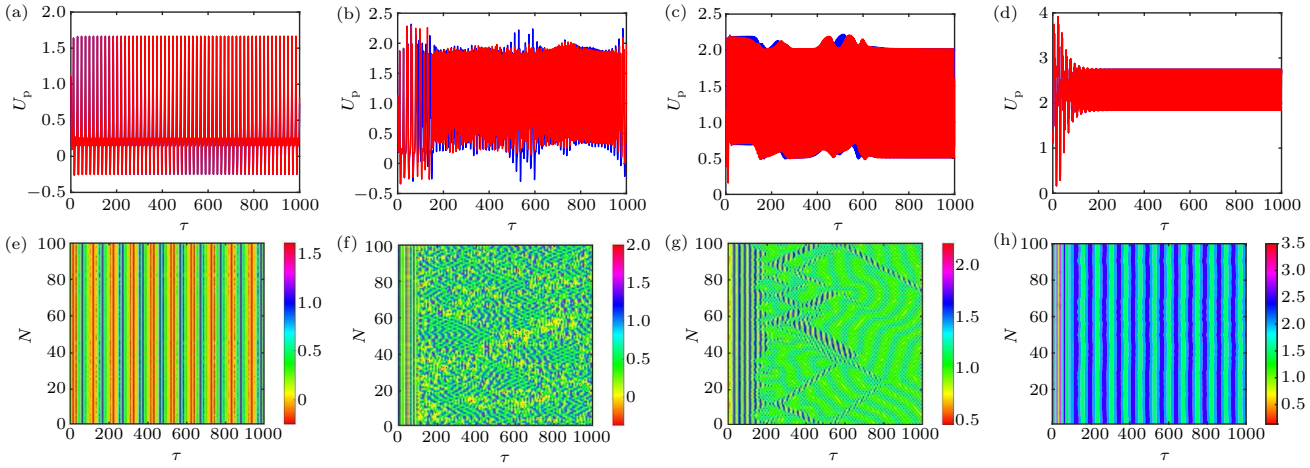


Fig. 5. Spatiotemporal patterns and time series of the memristive Josephson junction neuronal network for different values of the coupling parameter g_c. The selected values are $g_c = 0$, 0.1, 0.2, and 0.4. Other parameters are set as $\Gamma = 0.8$, $\lambda = 0.1$, $k_p = 0.06$, $i_{in} = 0.203$, $i_b = 1.909$, $v_s = 0$, and $\Lambda_s = 0.5$.

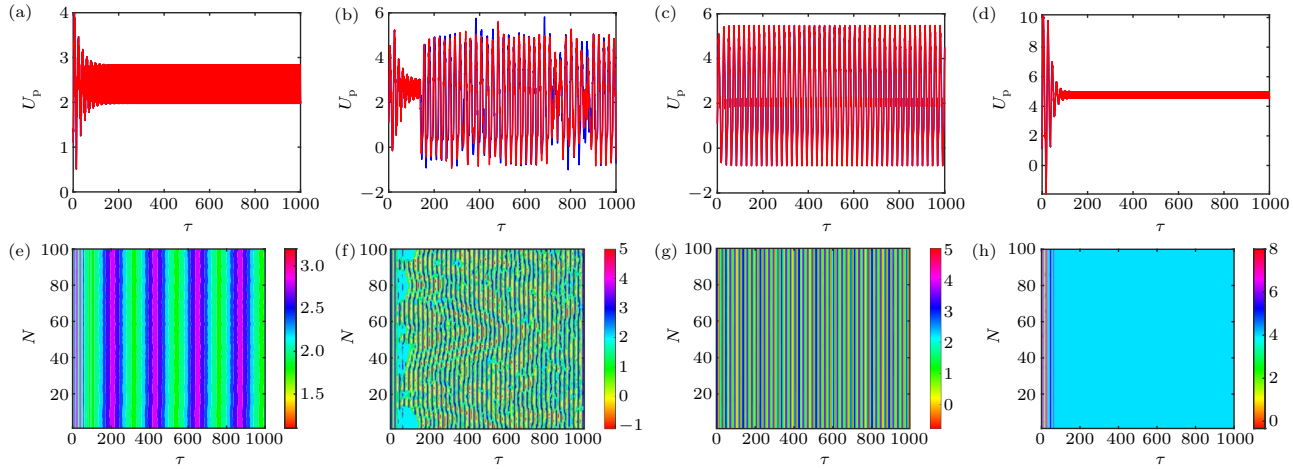


Fig. 6. Spatiotemporal patterns and time series of the memristive Josephson junction neuronal network for different values of the inhibitory bias voltage v_s. The selected values are $v_s = -0.1$, -0.3, -0.5, and -2.4. Other parameters are set as $\Gamma = 0.8$, $\lambda = 0.1$, $\Lambda_p = 0.5$, $i_{in} = 0.203$, $i_b = 1.909$, $g_c = 0.4$, $k_p = 0.06$, and $\Lambda_s = 0.5$.

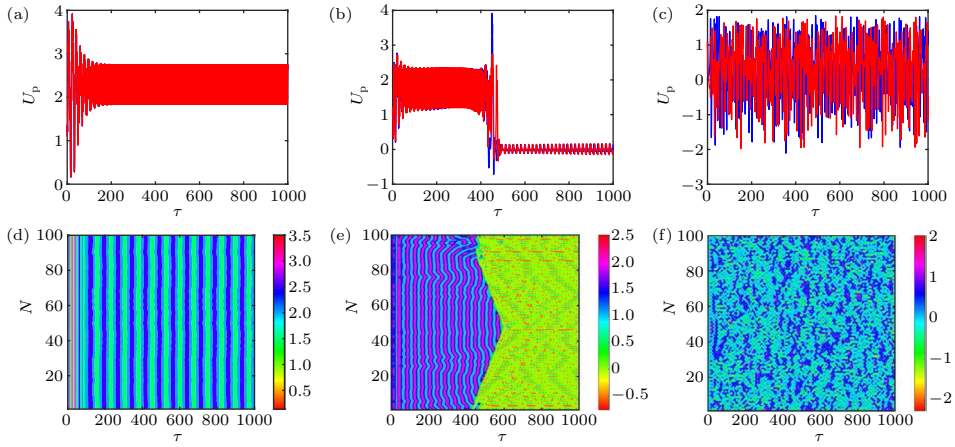


Fig. 7. Spatiotemporal patterns and time series of the memristive Josephson junction neuronal network for different values of the excitatory bias voltage v_s. The selected values are $v_s = 0$, 0.48, and 2.0. Other parameters are set as $\Gamma = 0.8$, $\lambda = 0.1$, $\Lambda_p = 0.5$, $i_{in} = 0.203$, $i_b = 1.909$, $g_c = 0.4$, $k_p = 0.06$, and $\Lambda_s = 0.5$.

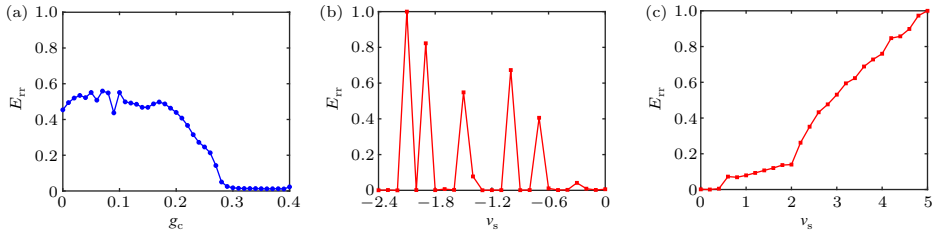


Fig. 8. Synchronization function diagrams of the memristive Josephson junction neuronal network. (a) Synchronization as a function of coupling strength g_c. (b) Synchronization as a function of synaptic reversal potential v_s in the range -2.4 to 0. (c) Synchronization as a function of synaptic reversal potential v_s in the range 0 to 5.

In summary, these results demonstrate that the appropriate coupling parameter g_c is crucial for the synchronization of neural networks. As g_c increases, the network gradually transitions from a disordered state to a fully synchronized state. This finding is of great significance for understanding and controlling the dynamic behavior of complex neural networks.

To further study the influence of the bias voltage parameter v_s on the synchronous dynamic behavior of the neural network, Fig. 6 shows the spatiotemporal patterns and time series of the memristive Josephson junction neuronal network under different values of v_s. The parameters v_s are set to -0.1, -0.3, -0.5, and -2.4, respectively, while the other parameters are set to $\Gamma = 0.8$, $\lambda = 0.1$, $\Lambda_p = 0.5$, $i_{in} = 0.203$, $i_b = 1.909$, $g_c = 0.4$, $k_p = 0.06$, and $\Lambda_s = 0.5$. In Figs. 6(a) and 6(e), at $v_s = -0.1$, the memristive Josephson junction neuronal network is in a synchronous state. As v_s increases to -0.3, Figs. 6(b) and 6(f) show that the network begins to exhibit more complex and irregular dynamic behavior. When v_s further increases to -0.5 and -2.4, the network undergoes a transition from periodic synchronization to resting synchronization. This phenomenon is consistent with the data shown in Fig. 4(b). These results are of great significance for understanding the dynamic characteristics of the memristive Josephson junction neuronal network and its behavior under different parameter conditions.

Figure 7 shows the spatiotemporal patterns and time series of the memristive Josephson junction neural network under different values of the parameter v_s. The parameter v_s in the figure is set to 0, 0.48, and 2, respectively, while other parameters are fixed as $\Gamma = 0.8$, $\lambda = 0.1$, $\Lambda_p = 0.5$, $i_{in} = 0.203$, $i_b = 1.909$, $g_c = 0.4$, $k_p = 0.06$, and $\Lambda_s = 0.5$. Observing the time series in Fig. 7(a) and the spatiotemporal diagram in Fig. 7(d), it can be seen that when $g_c = 0.4$ and $v_s = 0$, the memristive Josephson junction neural network system is in a stable synchronized state. As v_s increases to 0.48 (Figs. 7(b) and 7(e)), the network initially exhibits an unstable state, but its dynamic behavior becomes more regular at approximately 500 seconds. When the excitatory bias voltage further increases to 2, the amplitude and frequency of fluctuations in the time series grow, and the spatiotemporal pattern becomes significantly more complex, indicating increased diversity and complexity in the network dynamics. This process shows that increasing the excitatory bias voltage can lead to network desynchronization.

Next, we consider the synchronization of the memristive Josephson junction neuronal network with $k_p = 0.05$, which corresponds to the chaotic discharge mode.

Figure 8 details the influence of different parameters on the synchronization error when $k_p = 0.05$. When $k_p = 0.05$, the memristive Josephson junction system is in a chaotic state. Specifically, Fig. 8(a) illustrates the effect of the coupling conductance parameter g_c on the synchronization error. The figure shows that, as g_c increases, the synchronization error initially rises and then decreases, eventually approaching

zero. This trend suggests that appropriately increasing the coupling strength can effectively enhance network synchronization. Figure 8(b) shows the effect of the inhibitory bias voltage v_s on the synchronization error. The synchronization error exhibits noticeable irregular fluctuations with changes in v_s, indicating alternating synchronous and asynchronous states, which highlights the inhibitory bias voltage's critical role in controlling network synchronization. Figure 8(c) shows the effect of the excitatory bias voltage v_s on the synchronization error. The figure shows that increasing v_s leads to a gradual increase in synchronization error, indicating that higher excitatory bias voltage decreases network synchrony and makes synchronization harder to achieve. These results collectively reveal how different parameters affect synchronization error and help understand the network's synchronization behavior under varying conditions.

Figure 9 shows the spatiotemporal patterns and time series of the memristive Josephson junction neuronal network under different coupling strengths g_c. The parameters g_c in the figure are 0, 0.1, 0.2, and 0.4, while the other parameters are fixed as $\Gamma = 0.8$, $\lambda = 0.1$, $\Lambda_p = 0.5$, $i_{in} = 0.203$, $i_b = 1.909$, $v_s = 0$, $k_p = 0.05$, and $\Lambda_s = 0.5$. Figures 9(a)–9(d) show the changes in the voltage U_p over time τ. As g_c increases, network synchronization gradually improves. Figures 9(e)–9(h) show the spatiotemporal patterns of the neurons. As g_c increases, the color bars become vertically consistent, indicating that the network's spatiotemporal pattern transitions from disorder to order, exhibiting a more pronounced synchronization pattern. Overall, Fig. 9 highlights the significant influence of coupling strength g_c on the network's spatiotemporal dynamics, showing that appropriate coupling promotes synchronization.

Figure 10 shows the spatiotemporal patterns and time series of the memristive Josephson junction neuronal network under different values of v_s, with a fixed $g_c = 0.4$. The v_s values in the figure are -0.1, -0.5, -2.1, and -2.4, while the other parameters are fixed as $\Gamma = 0.8$, $\lambda = 0.1$, $\Lambda_p = 0.5$, $i_{in} = 0.203$, $i_b = 1.909$, $g_c = 0.4$, $k_p = 0.05$, and $\Lambda_s = 0.5$. Figures 10(a) and 10(e) show that the network exhibits more stable dynamics under smaller inhibitory bias voltage v_s. When v_s increases to -0.5, the network shows periodic synchronization. For $v_s = -2.1$, the network enters a chaotic non-synchronous state. When $v_s = -2.4$, the network is in a resting synchronization state. These results indicate that

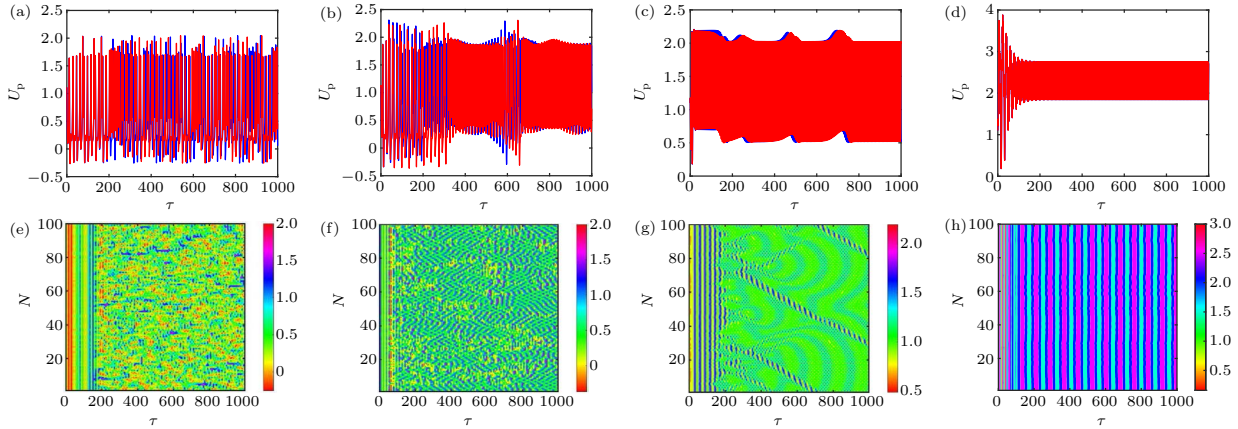


Fig. 9. Spatiotemporal patterns and time series of the memristive Josephson junction neuronal network for different values of the coupling strength g_c: 0, 0.1, 0.2, and 0.4. Other parameters are set as $\Gamma = 0.8$, $\lambda = 0.1$, $\Lambda_p = 0.5$, $i_{in} = 0.203$, $i_b = 1.909$, $v_s = 0$, $k_p = 0.05$, and $\Lambda_s = 0.5$.

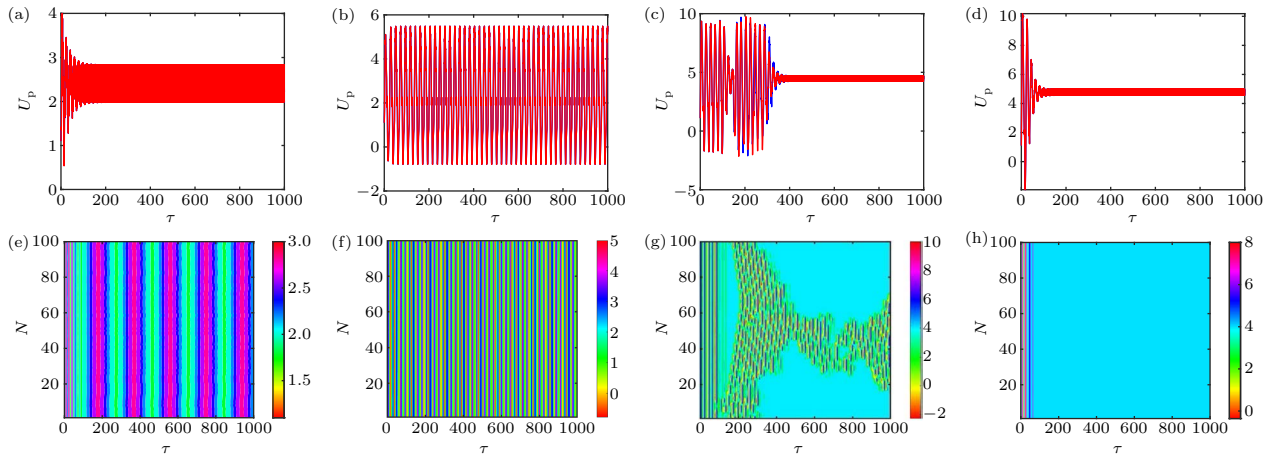


Fig. 10. Spatiotemporal patterns and time series of the memristive Josephson junction neuronal network for different values of the synaptic reversal potential v_s: -0.1, -0.5, -2.1, and -2.4. Other parameters are set as $\Gamma = 0.8$, $\lambda = 0.1$, $\Lambda_p = 0.5$, $i_{in} = 0.203$, $i_b = 1.909$, $g_c = 0.4$, $k_p = 0.05$, and $\Lambda_s = 0.5$.

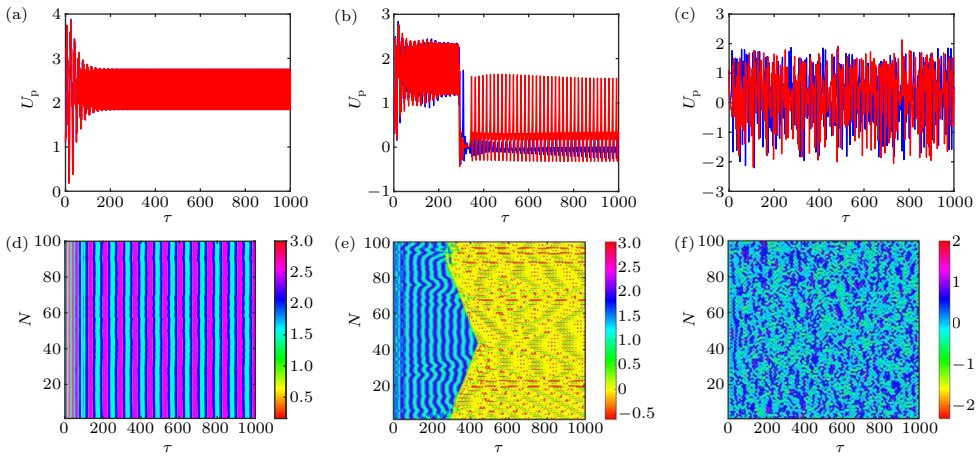


Fig. 11. Spatiotemporal patterns and time series of the memristive Josephson junction neuronal network for different values of the synaptic reversal potential v_s: 0, 0.49, and 2. Other parameters are set as $\Gamma = 0.8$, $\lambda = 0.1$, $\Lambda_p = 0.5$, $i_{in} = 0.203$, $i_b = 1.909$, $g_c = 0.4$, $k_p = 0.05$, and $\Lambda_s = 0.5$.

varying the inhibitory bias voltage v_s significantly affects network dynamics, inducing a range of behaviors from stable to periodic synchronization, then to chaotic non-synchronization, and finally to resting synchronization. Overall, Fig. 10 demonstrates the important influence of v_s on spatiotemporal network dynamics and shows that network synchronization can be effectively regulated by adjusting v_s. These findings enhance our understanding of network dynamics and provide theoretical support for designing networks with specific dynamic behaviors.

Figure 11 shows the spatiotemporal patterns and time series of the network under different values of the excitatory bias voltage parameter v_s. The parameters are selected as $v_s = 0$, 0.49, and 2, respectively, while the other parameters are fixed as $\Gamma = 0.8$, $\lambda = 0.1$, $\Lambda_p = 0.5$, $i_{in} = 0.203$, $i_b = 1.909$, $g_c = 0.4$, $k_p = 0.05$, and $\Lambda_s = 0.5$. The memristive Josephson junction neuronal network maintains a stable synchronized state without applying an excitatory bias voltage. However, when the excitatory bias voltage is slightly increased to $v_s = 0.49$, the network synchronization begins to be disturbed. Further increasing the excitatory bias voltage to $v_s = 2$, the time series diagram shows pronounced fluctuations, while the spatiotemporal pattern exhibits disordered color changes. At this stage, network synchronization is significantly disrupted, and the system enters an asynchronous state. This finding underscores the pivotal role of the excitatory bias voltage in controlling network synchronization. It reveals that even small voltage changes can induce substantial alterations in the network's dynamic behavior within a specific parameter range. These results indicate that network synchronization can be effectively regulated by adjusting v_s. In particular, a larger v_s value can destroy network synchronization. These findings not only deepen our understanding of the dynamic behavior of such networks but also provide essential theoretical support and practical guidance for designing and optimizing neural networks with specific dynamic characteristics.

4. Color image DNA encryption and decryption algorithm

In this section, image encryption is implemented by using the improved Josephson junction neuron model, DNA encoding and decoding, column replacement, and global pixel diffusion. The following is a flowchart illustrating the implementation of image encryption and decryption.

4.1. Color image DNA encryption algorithm

The improved neuron model is applied to the practical application of image encryption, and dynamic DNA coding is integrated to construct the image encryption algorithm. The specific process is as follows.

Step 1 Image preprocessing and blocking: read the plaintext image I with total dimensions $M \times N$. Divide the plaintext image into three two-dimensional matrices (I_1, I_2, I_3) in a hierarchical manner. To ensure consistent block sizes during encryption, divide the image into fixed-size blocks of size t. If the original image size cannot be evenly divided by the block size t, pad the image matrix with zeros to extend its boundaries, ensuring all image blocks have identical dimensions.

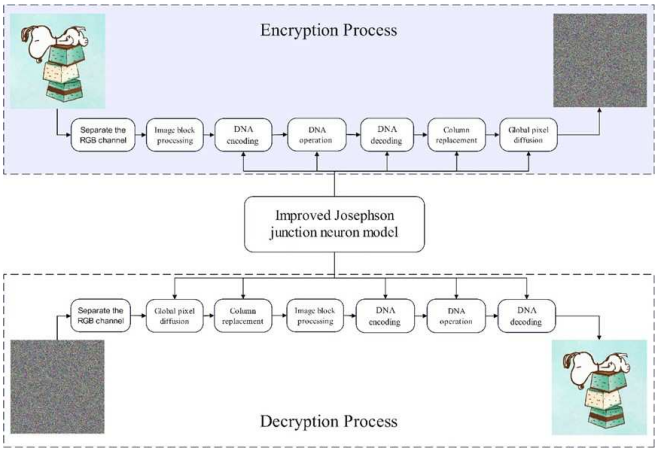


Fig. 12. Flow chart for the proposed cryptosystem.

Step 2 Generate the initial values of the chaotic system: based on the processed image block data in step 1, calculate the initial values of the system state variables of the improved Josephson junction neuron model.

Step 3 Dynamic DNA encoding and computation: using the initial values X_0, Y_0, Z_0, and H_0 generated in step 2, combined with the improved Josephson junction neuron model, we employ MATLAB's ode45 adaptive ODE solver for high-precision numerical computation. This process generates four pseudo-random chaotic sequences (denoted as $\{X_i\}$, $\{Y_i\}$, $\{Z_i\}$, and $\{H_i\}$), which serve distinct control functions during the encryption process.

To ensure encryption efficiency, the sequence $\{X_i\}$-controlled I_i (where $i = 1,2,3$) employs identical DNA encoding methods for blocks with matching positions. The $\{X_i\}$ sequence is mapped to an integer range $[1,8]$, corresponding to eight DNA encoding rules. Subsequently, the sequence $\{X_i\}$ is rounded and subjected to a 256-bit modulo operation to convert it into a one-dimensional sequence P. This is then transformed into a two-dimensional matrix R of the same size as I_1, with values normalized to 0–255 for DNA operations. The DNA encoding method for the R matrix under the $\{Y_i\}$-controlled sequence follows the same mapping rules as $\{X_i\}$. Similarly, considering encryption efficiency, the sequence $\{Z_i\}$-controlled I_i (where $i = 1,2,3$) and corresponding matrix blocks implement four operation rules: addition when equal to 0, subtraction when equal to 1, XOR when equal to 2, and OR when equal to 3.

Step 4 Dynamic DNA decoding: after completing DNA computation, the matrix blocks processed in step 3 undergo DNA decoding. This stage uses the sequence $\{H_i\}$ generated by the improved Josephson junction neuron model as the decoding controller to determine the DNA decoding rules for the processed sub-blocks. The process begins by mapping elements from sequence $\{H_i\}$ into an integer range $[1,8]$, corresponding to one of eight possible DNA decoding schemes. The decoding rules maintain a strict dual relationship with the encoding phase to ensure reversibility. Based on the selected decoding rules, the system converts DNA base sequences (A/G/C/T) into corresponding numerical matrices (pixel values within the 0–255 range), thereby completing the DNA decoding process.

Step 5 Column replacement: to achieve enhanced scrambling effects, the sequence $\{H_i\}$ generated by the chaotic system is sorted in descending order while recording each element's original position within the sequence. This process yields two new positional sequences U_x and U_y. The values of these sequences, along with their corresponding indices, are used as row-column swap coordinates. By applying these coordinates to the matrices of the three channels processed in step 4, we obtain the matrices II_1, II_2, and II_3 through matrix transposition.

Step 6 Global pixel diffusion: perform bidirectional global pixel diffusion on matrices II_1, II_2, and II_3.

Step 6.1 First perform forward diffusion. Taking matrix II_1 as an example, starting from the top-left pixel $II_1(1,1)$ and scanning in row-first order to the bottom-right pixel, the intermediate encrypted value $C(i,j)$ of each pixel is determined by combining the current plaintext pixel $II_1(i,j)$, key $K_1(i,j)$, and the previous pixel's calculated result C_1. The intermediate encryption value of each pixel is defined as $C(i,j) = II_1(i,j) \oplus K_1(i,j) \oplus C_1$, where C_1 typically takes the value $C(i,j-1)$ (in the same row) or $C(i-1,N)$ (at the end of the previous row). K_1 is generated through the chaotic sequence Y_i produced by the improved Josephson junction neuron model, forming a key matrix of the same size as the image. K_2 is generated from the chaotic sequence $\{Z_i\}$, forming another key matrix of equal size. For $C(1,1)$, the formula is $C(1,1) = II_1(1,1) \oplus K_1(1,1) \oplus (K_2(1,1) \oplus K_2(M,N))$.

Step 6.2 Forward diffusion alone is insufficient as it cannot propagate changes from the image's edges forward. To address this, we introduce a reverse diffusion phase. This stage takes the intermediate result matrix C from forward diffusion as input and scans backward from the bottom-right pixel to the top-left pixel $C(1,1)$. The final encrypted value $E(i,j)$ for each pixel is determined by three components: the intermediate value $C(i,j)$, the key $K_2(i,j)$, and the subsequent pixel's calculated result E_1. The final encrypted value of each pixel is defined as $E(i,j) = C(i,j) \oplus K_2(i,j) \oplus E_1$, where E_1 typically takes the value $E(i,j+1)$ or $E(i+1,1)$.

Step 7 Combine three channels R, G, B: the three matrices from step 6 are merged into a three-dimensional matrix to obtain the encrypted image.

4.2. Color image DNA decryption algorithm

Step 1 Encrypted image reading and layering: read the encrypted image and divide it into three two-dimensional matrices in a hierarchical manner.

Step 2 Generate chaotic sequences: use the same initial values X_0, Y_0, Z_0, and H_0 as in the encryption process to generate four sequences $\{X_i\}$, $\{Y_i\}$, $\{Z_i\}$, and $\{H_i\}$ through the improved Josephson junction neuron model.

Step 3 Global bidirectional reverse diffusion: perform global pixel inverse diffusion on the three matrices from step 1.

Step 4 Global pixel reverse scrambling: perform inverse row and column substitution on the matrices from step 3.

Step 5 Dynamic DNA encoding: perform DNA encoding on the sub-blocks from step 4. Use $\{H_i\}$ to determine the DNA encoding method for the sub-blocks of the encrypted image matrix. The generation method of the R matrix is identical to that used in encryption.

Step 6 DNA inverse operation: perform DNA inverse operations on the three matrices from step 5 using the corresponding blocks in the R matrix. During encryption and decryption, the operations are mutually inverse. Specifically, the addition, XOR, and OR operations used during encryption are reversed to subtraction, OR, and XOR operations during decryption, respectively.

Step 7 Dynamic DNA decoding: perform DNA decoding on the three matrices from step 6.

Step 8 Image reconstruction and output: remove the 0 pixels added during encryption, then merge the matrices into a three-dimensional matrix to obtain the decrypted color image.

4.3. Performance analysis of encryption security

4.3.1. Analysis of inter-adjacent pixel correlation

Generally, pixels are highly correlated with their neighbors. This connection is a critical vulnerability, as it can leak information and expose the image to statistical attacks. A robust encryption scheme must eliminate this pixel-to-pixel correlation. Its value range is $[-1,1]$, and the quality of the algorithm depends on how close the correlation coefficient is to zero. To measure this, we selected 5000 pairs of adjacent pixels from an original image and its encrypted version, then calculated the correlation coefficients for each using the following formula:

$$\begin{cases} R_{xy} = \dfrac{\operatorname{cov}(x,y)}{\sqrt{D(x)}\sqrt{D(y)}}, \\ E(x) = \dfrac{1}{N}\displaystyle\sum_{i=1}^{N} x_i, \\ D(x) = \dfrac{1}{N}\displaystyle\sum_{i=1}^{N} (x_i - E(x))^2, \\ \operatorname{Cov}(x,y) = \dfrac{1}{N}\displaystyle\sum_{i=1}^{N} (x_i - E(x))(y_i - E(y)), \end{cases} \tag{9}$$

where N is the total number of pixels in the image, $\operatorname{Cov}(x,y)$ is the covariance between pixel x and y, representing the correlation between two adjacent pixels, and $D(x)^{1/2}$ and $E(x)$ are the standard deviation and mean of all elements in the image, respectively.

Figure 13 shows the correlation scatter distribution of adjacent pixels in the R, G, and B channels of the Dog image in horizontal, vertical, and diagonal directions: the upper row shows the original image, with scatter points obviously clustered along the diagonal; the lower row shows the encrypted image, with scatter points approximately evenly distributed, without obvious linear structure. The adjacent pixels of the original image show strong correlation in all three directions, whereas the correlation of adjacent pixels of the encrypted image is significantly weakened to near zero. This demonstrates that the encryption process effectively breaks the neighborhood correlation of the image and improves its resistance to statistical and correlation analysis attacks.

Table 1. Correlation analysis.

Algorithm	Image	Horizontal	Vertical	Diagonal
Proposed	Dog	−0.0009	−0.0016	0.0055
	Minions	0.0079	0.0005	−0.0038
	Fruit	0.0007	−0.0056	−0.0046
Ref. [47]	image	−0.0072	0.0258	−0.0098
Ref. [48]	image	−0.0031	0.0097	0.0005
Ref. [49]	image	0.0167	0.1567	0.0090
Ref. [50]	image	0.0040	0.0148	0.0068

Table 1 shows the comparison of correlation coefficients of different algorithms in three adjacent pixel directions (horizontal, vertical, diagonal). For our algorithm, we list the results using three images — Dog, Minions, and Fruit — as examples, and compare them with results reported in Refs. [47–50]. As shown in Table 1, the correlation

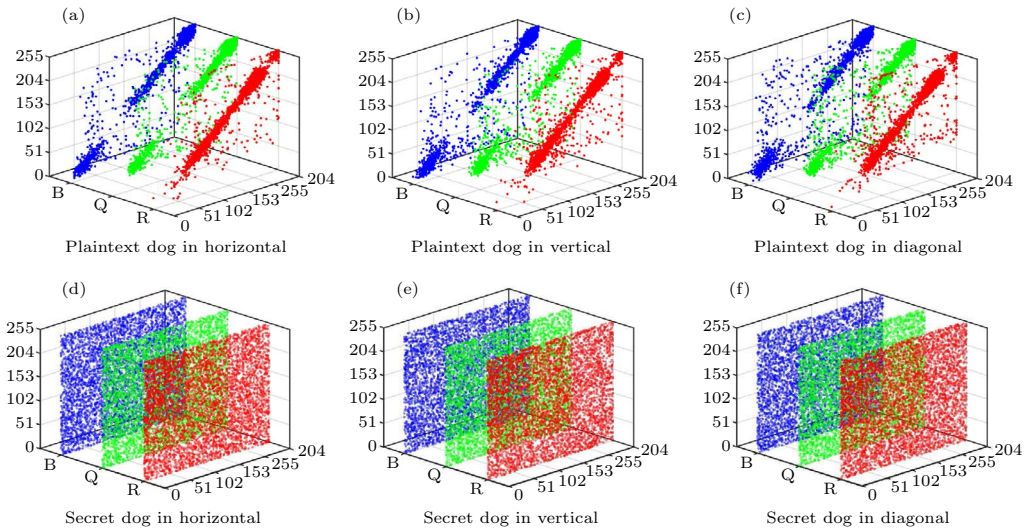


Fig. 13. Correlation between adjacent pixels in the Dog image. (a)–(c) Correlation maps of the R, G, and B channels for the original image in the horizontal, vertical, and diagonal directions; (d)–(f) Correlation maps of the R, G, and B channels for the encrypted image in the horizontal, vertical, and diagonal directions.

coefficients of our algorithm in all three directions are close to 0 and remain stable across the three test images, with the absolute value reaching about 0.0079 (horizontal direction of Minions). In contrast, the comparison methods exhibit significantly higher correlation, especially in the diagonal direction. Therefore, the quantitative results in Table 1 are consistent with the visual observations shown in Fig. 13.

4.3.2. Analysis of information entropy

Information entropy quantifies the randomness of a signal. When applied to an image, it measures how evenly the grayscale values are distributed within each color channel. We calculate the information entropy using the following formula:

$$H(x) = -\sum_{i=1}^{L} P(x_i)\log_2 P(x_i), \tag{10}$$

where x_i is the gray value of the i-th pixel of the image x, and $P(x_i)$ is the probability of occurrence of this gray value. As shown in Table 2, the information entropy of the three images is very close to the ideal value of 8. Compared with other algorithms, the encryption method proposed in this work demonstrates higher randomness and enhanced security.

Table 2. Information entropy analysis

Algorithm	Image	Encrypted images		
		R	G	B
Proposed	Dog	7.9994	7.9992	7.9993
	Minions	7.9993	7.9994	7.9993
	Fruit	7.9993	7.9994	7.9993
Ref. [50]	image	7.9982	7.9985	7.9984
Ref. [51]	image	7.9990	7.9990	7.9990

Table 2 presents the information entropy analysis results of different algorithms on three test images, showing the entropy values of the encrypted images on the R, G, and B channels, respectively. As observed from Table 2, the information entropy of our algorithm for all three channels across the three images is close to the theoretical ideal value of 8, ranging specifically between 7.9992 and 7.9994, which nearly matches an ideal random distribution. In contrast, the information entropy of other algorithms is generally slightly lower; for example, the results reported in Refs. [50,51] range from 7.9982 to 7.9990, showing a certain deviation from the ideal value. These results indicate that our algorithm achieves superior uniformity and randomness of pixel distribution, effectively enhancing the unpredictability and security of the encrypted images.

4.4. NPCR and UACI

In image encryption, it is crucial to verify that the algorithm can effectively resist differential attacks. A secure scheme should ensure that a minor change in the plaintext image leads to a significant difference in the corresponding cipher image. To quantify this property, two commonly used metrics are the number of pixels change rate (NPCR) and the unified average changing intensity (UACI), defined as follows:

$$\mathrm{NPCR} = \frac{\sum_{i,j} D(i,j)}{M \times N} \times 100\%, \tag{11}$$

where $D(i,j)$ is defined as

$$D(i,j) = \begin{cases} 1, & C_1(i,j) \neq C_2(i,j), \\ 0, & \text{otherwise}, \end{cases} \tag{12}$$

and the UACI is calculated by

$$\mathrm{UACI} = \frac{1}{M \times N} \frac{\sum |C_1(i,j) - C_2(i,j)|}{255} \times 100\%, \tag{13}$$

where C_1 and C_2 correspond to the cipher images generated from two plaintexts differing by a single pixel.

The ideal values for NPCR and UACI are 0.9961 and 0.3346, respectively. The closer these metrics are to their ideal theoretical values, the higher the encryption algorithm's sensitivity to key changes and the stronger its overall cryptographic robustness and reliability. Table 3 presents the average NPCR and UACI values obtained by our proposed method compared with other existing state-of-the-art encryption algorithms. The results clearly demonstrate that the proposed image encryption algorithm exhibits superior resistance to differential attacks and practical security threats.

Table 3. Sensitivity test.

	NPCR	UACI
Dog	0.99613	0.33456
Minions	0.99610	0.33465
Fruit	0.99613	0.33466
Ref. [47]	0.99618	0.33456
Ref. [50]	0.99652	0.33524
Ref. [52]	0.99615	0.33509

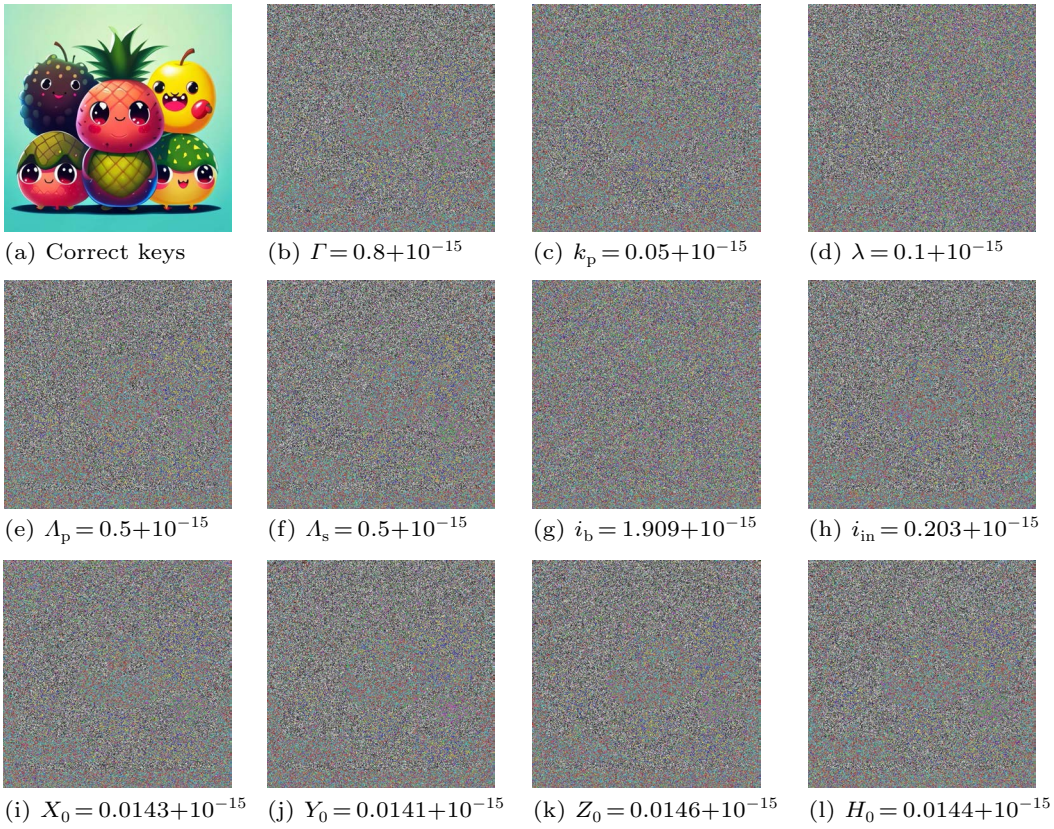
Specifically, Table 3 shows the performance of different algorithms in image sensitivity testing, mainly assessing the encryption algorithm's response to very small changes in the plaintext via NPCR and UACI metrics. As seen in Table 3, the NPCR value of our algorithm across the three test images is approximately 0.9960, and the UACI value is about 0.3346, both very close to the theoretical ideal values and consistently stable across different images under various testing conditions. Compared with the methods reported in the literature, the NPCR and UACI values of our algorithm are closer to the ideal, indicating that our method is more sensitive to even minor changes in the plaintext. Even extremely small pixel modifications in the original image lead to significant changes in the ciphertext, effectively resisting differential attacks and further ensuring the practical security and overall robustness of the encryption algorithm.

4.4.1. Analysis of key space

In image encryption, the key space of an algorithm is a critical factor in determining its resistance to exhaustive (brute-force) attacks. The key space of the proposed algorithm primarily consists of the system's fixed parameters Γ, k_{p}, λ, Λ_{p}, Λ_{s}, i_{b}, i_{in}, as well as the initial values of the chaotic sequences X_0, Y_0, Z_0, and H_0. All these parameters are specified with a precision of 10^{15}. Therefore, the size of the key space can be estimated as $10^{15\times 11} \approx 2^{546}$. Compared with other algorithms, the proposed method offers significantly stronger resistance to exhaustive attacks in practical real-world applications.

4.4.2. Analysis of key sensitivity

Key sensitivity is essential for an effective encryption algorithm, as it ensures that small changes in the key lead to significant changes in the decrypted image, thus preventing unauthorized decryption. In this section, the sensitivity of the proposed algorithm is analyzed. When the correct key is applied, the ciphertext image is successfully decrypted. However, when a minor perturbation is introduced to a single key parameter and decryption is attempted again, the resulting image, as shown in Fig. 14, fails to recover the original information. This demonstrates that the proposed algorithm is highly sensitive to the key, which effectively prevents attacks and further strengthens its security against exhaustive searches.



(a) Correct keys (b) $\Gamma = 0.8+10^{-15}$ (c) $k_{\mathrm{p}} = 0.05+10^{-15}$ (d) $\lambda = 0.1+10^{-15}$

(e) $\Lambda_{\mathrm{p}} = 0.5+10^{-15}$ (f) $\Lambda_{\mathrm{s}} = 0.5+10^{-15}$ (g) $i_{\mathrm{b}} = 1.909+10^{-15}$ (h) $i_{\mathrm{in}} = 0.203+10^{-15}$

(i) $X_0 = 0.0143+10^{-15}$ (j) $Y_0 = 0.0141+10^{-15}$ (k) $Z_0 = 0.0146+10^{-15}$ (l) $H_0 = 0.0144+10^{-15}$

Fig. 14. Decryption effect with different keys.

4.4.3. Histogram analysis

Raw digital images, as collections of pixels, typically exhibit significant unevenness and discernible statistical patterns in their pixel value distributions. To effectively resist statistical attacks exploiting these patterns, an ideal encrypted image should have a pixel value distribution that is as uniform as possible. In this context, the histogram — a graphical representation that intuitively displays the distribution of pixel values — serves as an essential tool for evaluating the uniformity of encrypted images. Consequently, histogram analysis has become a widely adopted metric for assessing an image's resistance to statistical attacks.

Figure 15 illustrates the effects of encryption and decryption on the Fruit image. Panels (a), (b), and (c) correspond to the original image, the encrypted image, and the decrypted image, respectively. Panels (d)–(f) show the histograms of the original image's R, G, and B channels, revealing that pixel values are highly concentrated in specific ranges, reflecting strong statistical features. In contrast, panels (g)–(i) present the histograms of the encrypted image, where the pixel values in each channel are approximately uniformly distributed across the full 0–255 range.

As can be observed from Fig. 15, the encrypted image visually loses all recognizable features of the original image, appearing as random noise, while the decrypted image successfully restores the original content, demonstrating correct reversibility. The histogram comparison further confirms that

the encryption algorithm effectively eliminates the statistical features of the original image, achieving near-ideal uniform distribution of pixel values and thereby enhancing the randomness and security of the encrypted image.

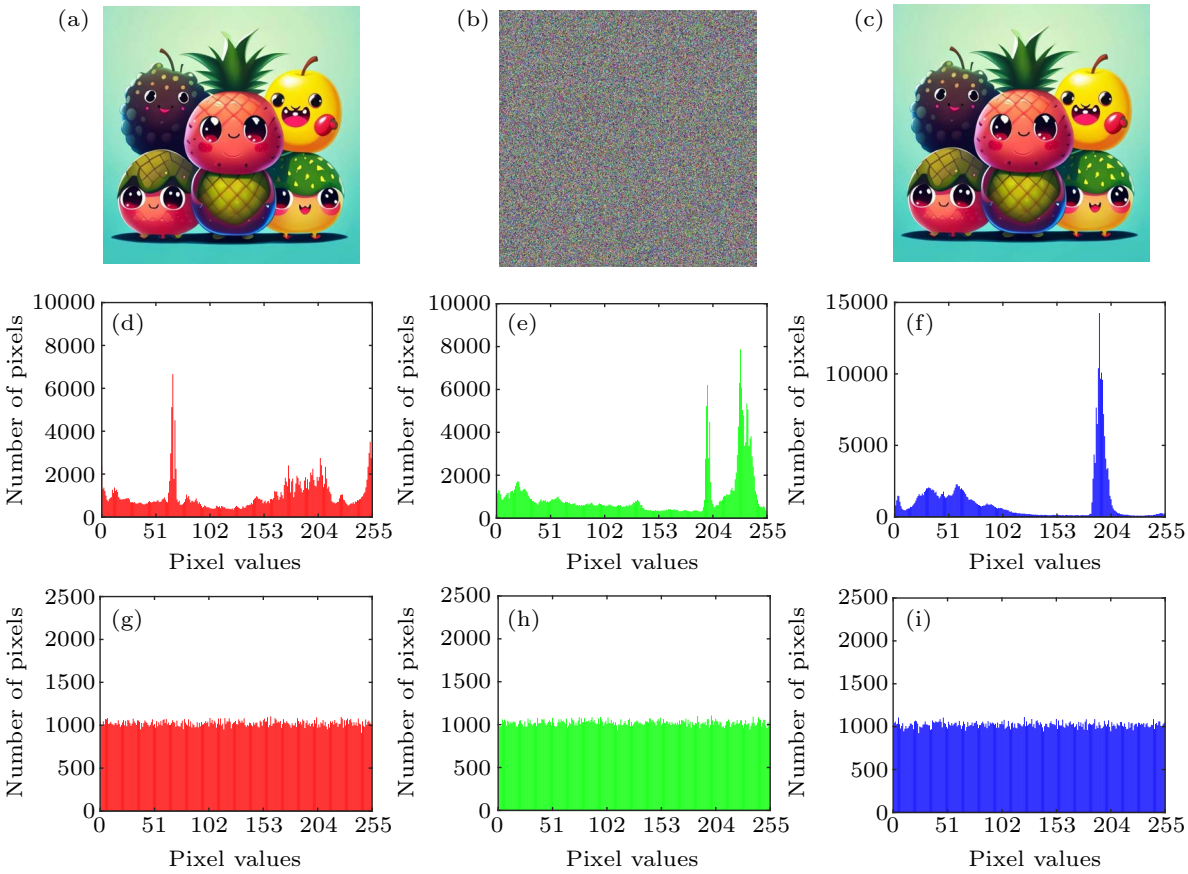


Fig. 15. Analysis of the fruit image encryption and decryption. (a) Plaintext image, (b) encrypted image, (c) decrypted image; (d)–(f) histograms of the R, G, and B channels of the plaintext image, showing uneven pixel distribution; (g)–(i) histograms of the R, G, and B channels of the encrypted image, illustrating uniform pixel distribution and enhanced randomness.

5. Conclusion

In this study, we proposed and constructed a memristive Josephson junction neuron model. Through numerical simulations of bifurcation diagrams, time series, and phase trajectories, we systematically investigated the model's dynamic characteristics. The results demonstrate that by adjusting key parameters, the model exhibits a variety of nonlinear dynamic behaviors, including periodic discharge, period-doubling bifurcations, and chaotic discharge.

Based on the single-neuron model, a coupled network system was further constructed to analyze how the conductance coupling parameter and the bias voltage influence the collective dynamics. Our findings indicate that the coupling parameter plays a crucial role in network synchronization.

Leveraging the complex chaotic sequences generated by the model, a novel DNA-based color image encryption algorithm was designed and implemented. Security analyses show that the algorithm possesses a large key space, exhibits high sensitivity to initial conditions, effectively resists differential and statistical attacks, and provides strong encryption security. These results suggest potential applications in secure communication and neuromorphic computing systems.

The current work primarily focuses on theoretical modeling, network synchronization analysis, and numerical simulations, without physical circuit fabrication or experimental verification. Future efforts will involve collaboration with experimental teams to realize the proposed memristive Josephson junction circuits, referencing existing hardware frameworks in neuromorphic systems. Additionally, the current model has been applied only to color image DNA encryption; its extension to other applications, such as real-time sensor data processing or engineering-oriented estimation tasks in hybrid neuromorphic computing systems,[53–55] remains to be explored.

Network scalability is another limitation: the present study considers a 100-neuron chain structure, while larger networks comprising hundreds or thousands of neurons with diverse topologies (e.g., star or scale-free networks) have not yet been investigated. Future research will examine the effects of large-scale networks and various topologies on dynamic behaviors and synchronization patterns.

Appendix A

To analyze the equilibrium points of the memristive Josephson junction neuron-like system, we define

$$\dot{\theta}_{\rm p} = \omega_{\rm p}, \quad \dot{\theta}_{\rm c} = \omega_{\rm c}, \tag{A1}$$

which transforms the original system in Eq. (6) into

$$\dot{\theta}_{\rm p} = \omega_{\rm p}, \tag{A2}$$

$$\dot{\omega}_{\rm p} = -\Gamma(1+k_{\rm p}\cos\theta_{\rm p})\omega_{\rm p} - \sin\theta_{\rm p} - \lambda(\theta_{\rm p}+\theta_{\rm c}) + \Lambda_{\rm s} i_{\rm in} + (1-\Lambda_{\rm p}) i_{\rm b}, \tag{A3}$$

$$\dot{\theta}_{\rm c} = \omega_{\rm c}, \tag{A4}$$

$$\dot{\omega}_{\rm c} = -\Gamma(1+k_{\rm p}\cos\theta_{\rm c})\omega_{\rm c} - \sin\theta_{\rm c} - \lambda(\theta_{\rm p}+\theta_{\rm c}) + \Lambda_{\rm s} i_{\rm in} - \Lambda_{\rm p} i_{\rm b}. \tag{A5}$$

Setting

$$\dot{\theta}_{\rm p} = \dot{\theta}_{\rm c} = 0, \tag{A6}$$

the equilibrium point of the system is $(\theta_{\rm p}^*, 0, \theta_{\rm c}^*, 0)$, where $\theta_{\rm p}^*$ and $\theta_{\rm c}^*$ are determined by

$$\sin\theta_{\rm p}^* - \sin\left(-\frac{\sin\theta_{\rm p}^*}{\lambda} - \theta_{\rm p}^* + \frac{\Lambda_{\rm s} i_{\rm in} + (1-\Lambda_{\rm p}) i_{\rm b}}{\lambda}\right) = i_{\rm b}, \tag{A7}$$

$$\theta_{\rm c}^* = \frac{-\sin\theta_{\rm p}^* + \Lambda_{\rm s} i_{\rm in} + (1-\Lambda_{\rm p}) i_{\rm b}}{\lambda} - \theta_{\rm p}^*. \tag{A8}$$

To investigate the local dynamics near the equilibrium point, the Jacobian matrix is given by

$$J = \begin{bmatrix} 0 & 1 & 0 & 0 \\ A & B & -\lambda & 0 \\ 0 & 0 & 0 & 1 \\ -\lambda & 0 & A & B \end{bmatrix}, \tag{A9}$$

with

$$\begin{cases} A = k_{\rm p}\omega_{\rm c}\Gamma\sin\theta_{\rm c} - \cos\theta_{\rm c} - \lambda, \\ B = -\Gamma(1+k_{\rm p}\cos\theta_{\rm c}). \end{cases} \tag{A10}$$

The characteristic polynomial is

$$f(\mu) = a\mu^4 + b\mu^3 + c\mu^2 + d\mu + e = 0, \tag{A11}$$

where

$$\begin{cases} a = 1, \\ b = \Gamma(k_{\rm p}\cos\theta_{\rm p} + k_{\rm p}\cos\theta_{\rm c} + 2), \\ c = 2\lambda + \cos\theta_{\rm c} + \cos\theta_{\rm p} + \Gamma^2(1+k_{\rm p}\cos\theta_{\rm c})(1+k_{\rm p}\cos\theta_{\rm p}) \\ \quad - \Gamma k_{\rm p}(\omega_{\rm c}\sin\theta_{\rm c} + \omega_{\rm p}\sin\theta_{\rm p}), \\ d = \Gamma\lambda(2 + k_{\rm p}(\cos\theta_{\rm p} + \cos\theta_{\rm c})) + \Gamma(\cos\theta_{\rm c} + \cos\theta_{\rm p}) \\ \quad + 2\Gamma k_{\rm p}\cos\theta_{\rm p}\cos\theta_{\rm c} - \Gamma^2 k_{\rm p}(\omega_{\rm c}\sin\theta_{\rm c} + \omega_{\rm p}\sin\theta_{\rm p}) \\ \quad - \Gamma^2 k_{\rm p}^2(\omega_{\rm c}\cos\theta_{\rm p}\sin\theta_{\rm c} + \omega_{\rm p}\cos\theta_{\rm c}\sin\theta_{\rm p}), \\ e = \cos\theta_{\rm c}\cos\theta_{\rm p} + \lambda(\cos\theta_{\rm p} + \cos\theta_{\rm c}) \\ \quad - \Gamma k_{\rm p}(\omega_{\rm c}\cos\theta_{\rm p}\sin\theta_{\rm c} + \omega_{\rm p}\cos\theta_{\rm c}\sin\theta_{\rm p}) \\ \quad - \Gamma k_{\rm p}\lambda(\omega_{\rm c}\sin\theta_{\rm c} + \omega_{\rm p}\sin\theta_{\rm p}) + \Gamma^2 k_{\rm p}^2\omega_{\rm c}\omega_{\rm p}\sin\theta_{\rm c}\sin\theta_{\rm p}. \end{cases} \tag{A12}$$

The roots of Eq. (A11) yield the eigenvalues

$$\begin{aligned} \mu_1 &= \frac{-b}{4} - \frac{1}{2}\sqrt{\frac{b^2}{4} - \frac{2c}{3} + \Delta} \\ &\quad - \frac{1}{2}\sqrt{\frac{b^2}{2} - \frac{4c^2}{3} - \Delta - \frac{b^3 + 4bc - 8d}{4\sqrt{\frac{b^2}{4} - \frac{2c}{3} + \Delta}}}, \\ \mu_2 &= \frac{-b}{4} - \frac{1}{2}\sqrt{\frac{b^2}{4} - \frac{2c}{3} + \Delta} \\ &\quad + \frac{1}{2}\sqrt{\frac{b^2}{2} - \frac{4c^2}{3} - \Delta - \frac{b^3 + 4bc - 8d}{4\sqrt{\frac{b^2}{4} - \frac{2c}{3} + \Delta}}}, \\ \mu_3 &= \frac{-b}{4} + \frac{1}{2}\sqrt{\frac{b^2}{4} - \frac{2c}{3} + \Delta} \\ &\quad - \frac{1}{2}\sqrt{\frac{b^2}{2} - \frac{4c^2}{3} - \Delta + \frac{b^3 + 4bc - 8d}{4\sqrt{\frac{b^2}{4} - \frac{2c}{3} + \Delta}}}, \\ \mu_4 &= \frac{-b}{4} + \frac{1}{2}\sqrt{\frac{b^2}{4} - \frac{2c}{3} + \Delta} \\ &\quad + \frac{1}{2}\sqrt{\frac{b^2}{2} - \frac{4c^2}{3} - \Delta + \frac{b^3 + 4bc - 8d}{4\sqrt{\frac{b^2}{4} - \frac{2c}{3} + \Delta}}}, \end{aligned} \tag{A13}$$

where $\{\mu_1, \mu_2, \mu_3, \mu_4\}$ as defined in the main text. Here,

$$\begin{cases} \Delta_1 = c^2 - 3bd + 12e, \\ \Delta_2 = 2c^3 - 9bcd + 27d^2 + 27b^2 e - 72ce, \\ \Delta = \frac{\sqrt[3]{2\Delta_1}}{3\sqrt[3]{\frac{\Delta_2 + \sqrt{-4\Delta_1^3 + \Delta_2^2}}{2}}} + \frac{\sqrt[3]{\frac{\Delta_2 + \sqrt{-4\Delta_1^3 + \Delta_2^2}}{2}}}{3\sqrt[3]{2}}. \end{cases} \tag{A14}$$

A key observation is that the damping parameter Γ does not appear in the equilibrium Eqs. (A7) and (A8), and thus does not affect the location of the fixed points. Furthermore, analysis of the eigenvalues in Eq. (A13) shows that Γ does not alter the sign of their real parts. Equation (A13) also explains why the system does not exhibit Hopf bifurcations. Since Γ corresponds to a positive damping coefficient, it cannot cross the real axis.

Consequently, the stability profile of the system is independent of Γ, although this parameter determines the qualitative nature of the fixed point, i.e., whether it manifests as a focus (complex eigenvalues) or a node.

Figure A1 illustrates the distribution of fixed points, where the system loses stability through saddle-and-yeast bifurcation lines (white). Our analysis indicates that the absolute value of $i_{\rm b}$ approaches zero as the number of fixed points increases, and the number of fixed points becomes zero when $|i_{\rm b}| > 2$. To accurately capture the origin of spike potential behavior, we set $i_{\rm b} = 1.909$.

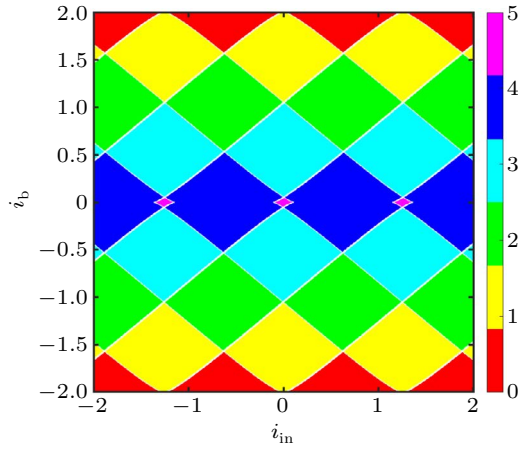


Fig. A1. Distribution of stable equilibrium points calculated from Eq. (A7) over the parameter domain $i_{in} \in (-2,2)$ and $i_b \in (-2,2)$. White lines indicate saddle-node bifurcation thresholds. Constant parameters are set as $\lambda = 0.1$ and $\Lambda_p = \Lambda_s = 0.5$.

Acknowledgments

The authors sincerely thank the editor, anonymous reviewers, and Huimin Qi for their valuable comments and suggestions that greatly improved this work. This research was supported by the National Natural Science Foundation of China (Grant No. 12302070), the Natural Science Foundation of Ningxia (Grant No. 2024AAC05002), the Youth Science and Technology Talent Cultivation Project of Ningxia, and the Ningxia Science and Technology Leading Talent Training Program (Grant No. 2022GKLRLX04).

References

[1] Ma J 2023 *J. Zhejiang Univ. Sci. A* **24** 109
[2] Lei Z and Ma J 2025 *Chaos* **35** 023158
[3] Jia J, Yang F and Ma J 2023 *Chaos Soliton Fract.* **173** 113689
[4] Feng X, Kang T and Wu F 2025 *Nonlinear Dyn.* **113** 13727
[5] Wan J, Wu F, Ma J and Wang W 2024 *Chin. Phys. B* **33** 050504
[6] Ge M, Jia Y, Xu Y and Yang L 2018 *Nonlinear Dyn.* **91** 515
[7] Zhang Y, Xu Y, Yao Z and Ma J 2020 *Nonlinear Dyn.* **102** 1849
[8] Qi H, Li F, Wang Q and Wu F 2025 *Chaos Solitons Fract.* **199** 116780
[9] Wu F and Wang R 2023 *Commun. Nonlinear Sci.* **126** 107459
[10] Wu F, Hu X and Ma J 2022 *Appl. Math. Comput.* **432** 127366
[11] Wu F, Gu H and Jia Y 2021 *Chaos Soliton Fract.* **153** 111611
[12] An X and Qiao S 2021 *Chaos, Soliton Fract.* **143** 110587
[13] Li K, Bao H, Li H, Ma J, Hua Z and Bao B 2022 *IEEE T. Ind. Inf.* **18** 1726
[14] Shao Y, Wu F and Wang Q 2024 *Nonlinear Dyn.* **112** 13483
[15] Shao Y, Wu F and Wang Q 2025 *Math. Comput. Simulat.* **233** 99
[16] Xu Q, Fang Y, Feng C, Parastesh F, Chen M and Wang N 2024 *Nonlinear Dyn.* **112** 13451
[17] Shao Y, Wu F and Wang Q 2025 *Nonlinear Dyn.*
[18] Tian X, Wu F and Ma J 2025 *Chaos Soliton Fract.* **199** 116828
[19] Josephson B D 1962 *Phys. Lett.* **1** 251
[20] Schegolev A E, Klenov N V, Gubochkin G I, Kupriyanov M Yu and Soloviev I I 2023 *Nanomaterials* **13** 2101
[21] Zhou J and Chen J 2021 *Adv. Elect. Materials* **7** 2100465
[22] Hens C, Pal P and Dana S K 2015 *Phys. Rev. E* **92** 022915
[23] Crotty P, Schult D and Segall K 2010 *Phys. Rev. E* **82** 011914
[24] Chalkiadakis D and Hizanidis J 2022 *Phys. Rev. E* **106** 044206
[25] Peotta S and Di Ventra M 2014 *Phys. Rev. Appl.* **2** 034011
[26] Wu F, Meng H and Ma J 2024 *Neural Networks* **169** 607
[27] Wu F, Guo Y, Ma J and Jin W 2023 *Appl. Math. Comput.* **455** 128131
[28] Wu F and Yao Z 2023 *Nonlinear Dyn* **111** 13481
[29] Zhang G, Wu F, Hayat T and Ma J 2018 *Commun. Nonlinear Sci.* **65** 79
[30] Yang F, Ma J and Ren G 2024 *J. Theor. Biol.* **578** 111686
[31] Hongray T, Balakrishnan J and Dana S K 2015 *Chaos* **25** 123104
[32] Wu F and Feng X 2025 *Nonlinear Dyn.*
[33] Segall K, LeGro M, Kaplan S, Svitelskiy O, Khadka S, Crotty P and Schult D 2017 *Phys. Rev. E* **95** 032220
[34] Vlasov V and Pikovsky A 2013 *Phys. Rev. E* **88** 022908
[35] Pfeiffer J, Schuster M, Abdumalikov A A and Ustinov A V 2006 *Phys. Rev. Lett.* **96** 034103
[36] Aranson I, Gitterman M and Shapiro B Y 1995 *Phys. Rev. B* **52** 12878
[37] Mishra A, Ghosh S, Kumar Dana S, Kapitaniak T and Hens C 2021 *Chaos* **31** 052101
[38] Domínguez D and Cerdeira H A 1995 *Phys. Rev. B* **52** 513
[39] Zhou T G, Yan S L, Fang L, He M and Zhao X J 2009 *Supercond. Sci. Technol.* **22** 055017
[40] Ma J, Wu F, Ren G and Tang J 2017 *Appl. Math. Comput.* **298** 65
[41] Bao H, Wang Z, Hua Z, Yu X, Xu Q and Bao B 2024 *IEEE T. Ind. Inf.* **20** 4784
[42] Chen M, Luo X, Zhang Y, Wu H, Xu Q and Bao B 2024 *IEEE T. Circuits Syst. I* **71** 781
[43] Zhang G, Ma J, Alsaedi A, Ahmad B and Alzahrani F 2018 *Appl. Math. Comput.* **321** 290
[44] Ramakrishnan B, Nkandeu Kamdeu P Y, Natiq H, Pone J R M, Karthikeyan A, Kingni S T and Tiedeu A 2022 *Multimed Tools Appl.* **81** 23819
[45] Ramakrishnan B, Tsafack N, Kemnang Tsafack A S, Tabekoueng Njitacke Z and Kingni S T 2022 *Pramana - J. Phys.* **96** 175
[46] Somers D and Kopell N 1993 *Biol. Cybern.* **68** 393
[47] Wang X and Zhao M 2021 *Opt. Laser Technol.* **143** 107316
[48] Folifack Signing V R, Fozin Fonzin T and Kountchou M 2021 *Circ. Syst. Signal. Pr.* **40** 4370
[49] Benssalah M, Rhaskali Y and Drouiche K 2021 *Multimed Tools Appl.* **80** 2081
[50] Es-sabry M, Akkad N E, Khrissi L, Satori K, Satori K, El-shafai W, Altameem T and Rathore R S 2024 *Egypt. Inform. J.* **25** 100449
[51] Li Q and Chen L 2024 *Multimed Tools Appl.* **83** 5351
[52] He C, Chen Z, Sun X and L Wang 2023 *IEEE Access* **11** 34163
[53] Ji X, Chen Y, Wang J, *et al.* 2024 *IEEE Internet. Things* **11** 39941
[54] Ji X, Dong Z, Zhou G, *et al.* 2024 *IEEE T. Syst. Man CyS.* **54** 5137
[55] Dong Z, Ji X, Wang J, *et al.* 2023 *IEEE T. Consum. Electr.* **70** 4311